ELSEVIER

● *Technical Note*

ACOUSTIC SHADOW DETECTION: STUDY AND STATISTICS OF B-MODE AND RADIOFREQUENCY DATA

RICKY HU,* ROHIT SINGLA,* FARAH DEEBA,* and ROBERT N. ROHLING*,†

* Department of Electrical and Computer Engineering, University of British Columbia, Vancouver, Canada; and † Department of Mechanical Engineering, University of British Columbia, Vancouver, Canada

Abstract—An acoustic shadow is an ultrasound artifact occurring at boundaries between significantly different tissue impedances, resulting in signal loss and a dark appearance. Shadow detection is important as shadows can identify anatomical features or obscure regions of interest. A study was performed to scan human participants (N = 37) specifically to explore the statistical characteristics of various shadows from different anatomy and with different transducers. Differences in shadow statistics were observed and used for shadow detection algorithms with a fitted Nakagami distribution on radiofrequency (RF) speckle or cumulative entropy on brightness-mode (B-mode) data. The fitted Nakagami parameter and entropy values in shadows were consistent across different transducers and anatomy. Both algorithms utilized adaptive thresholding, needing only the transducer pulse length as an input parameter for easy utilization by different operators or equipment. Mean Dice coefficients (± standard deviation) of 0.90 ± 0.07 and 0.87 ± 0.08 were obtained for the RF and B-mode algorithms, which is within the range of manual annotators. The high accuracy in different imaging scenarios indicates that the shadows can be detected with high versatility and without expert configuration. The understanding of shadow statistics can be used for more specialized techniques to be developed for specific applications in the future, including pre-processing for machine learning and automatic interpretation. (E-mail: rhu@ece.ubc.ca) Crown Copyright © 2019 Published by Elsevier Inc. on behalf of World Federation for Ultrasound in Medicine & Biology. All rights reserved.

Key Words: Acoustic shadow, Ultrasound, Speckle, Radiofrequency, Segmentation.

INTRODUCTION

Ultrasound devices have become increasingly affordable and portable, encouraging applications such as point-of-care ultrasound (Bouhemad et al. 2011), novice usage (Sippel et al. 2011) and analysis by machine learning (Ghose et al. 2013). However, ultrasound is susceptible to unique artifacts that increase the difficulty of interpretation and processing of images. One artifact is an acoustic shadow, which occurs when an ultrasound wave crosses a boundary of two materials with high impedance differences (Kremkau and Taylor 1986). The wave is almost completely reflected, and depicted beyond the boundary are a continuous dark region and a loss of anatomical features. Shadows occur in air−tissue, tissue−bone and tissue−lesion interfaces. Shadows can aid interpretation, such as identifying gall stones (Good et al. 1979) or spinal levels (Galiano et al. 2005).

However, shadows, such as from poor transducer contact, can lead to misinterpretation of anatomy, particularly by novice users and automated processing algorithms. Thus, the identification of shadows is an important pre-processing step in many applications.

Several methods described in the literature have been used to detect shadows, and illustrative examples are discussed. Geometric techniques model the path of an ultrasound signal for an expected image along the scanline using a random walk (Karamalis et al. 2012). Pixels are then flagged as a shadow if it is below a heuristic confidence threshold of 0.25. However, geometric techniques require knowledge of ultrasound transducer properties to parameterize random walk weights, such as the focal length, radius of curvature and thickness. The technique is therefore challenging to implement across different ultrasound equipment. This also reduces applicability for machine learning applications as accurate transducer parameter labels are required for each image.

Address correspondence to: Ricky Hu, Robotics and Control Laboratory, University of British Columbia, Room 3090, 2332 Main Mall, Vancouver, BC, Canada V6T 1Z4. E-mail: rhu@ece.ubc.ca

Pixel gray level methods ignore the transducer properties and analyze only the graphical properties of an image (Hellier et al. 2010). Shadows have been detected on brain images by analyzing the entropy along a scanline to flag pixels of sudden low entropy as a potential shadow. These techniques achieved a comparable Dice similarity coefficient as geometric methods, but require specific thresholding, window sizing, filtering and image mask parameterization for different anatomy and transducers. The drawback is again the need for parameterization and tuning, which requires image processing expertise and prior knowledge of specific applications.

Machine learning methods have become of significant interest in medical imaging analysis. To our knowledge, no machine learning method has demonstrated the capability of general shadow detection from multiple types of anatomy. Deep learning methods have identified features in specific image sets that contain shadows, such as neuroanatomical regions in a cranial scan (Milletari et al. 2017) or spinal levels in a posterior scan (Hetherington et al. 2017). Although machine learning has the potential to provide automated feature recognition in multiple applications, a large data set is required for an algorithm to recognize certain features. Ultrasound imaging is highly variable because of the unique artifacts, operator techniques and equipment. In addition, shadows are a common feature that occur in various imaging scenarios. Previous techniques focused on a single anatomical region, and training data were from a consistent imaging scenario. However, it is difficult to construct a training data set with the generality required to recognize shadows in different scenarios usable for a variety of ultrasound applications.

There were two objectives in the study described here. First, to address the need to understand the general characteristics of shadows, a study was conducted to scan multiple types of anatomy and transducers specifically to analyze the statistics of different types of shadows. Second, to address existing needs for versatile detection with minimal parameterization, previous methods were then extended utilizing statistical thresholding of radiofrequency (RF) or brightness-mode (B-mode) data to detect shadows from various imaging scenarios. The two methods are illustrated in the flowchart in Figure 1.

METHODS

Data collection

Ultrasound RF and B-mode data were acquired by scanning 37 adult participants with informed written consent, approved by the University of British Columbia Research Ethics Board (Study ID: H18-01199). The scans included a forearm scan near the distal end of the pronator quadratus, an elbow scan near the cubital fossa and a rib scan on the anterior surface of right ribs 11 and
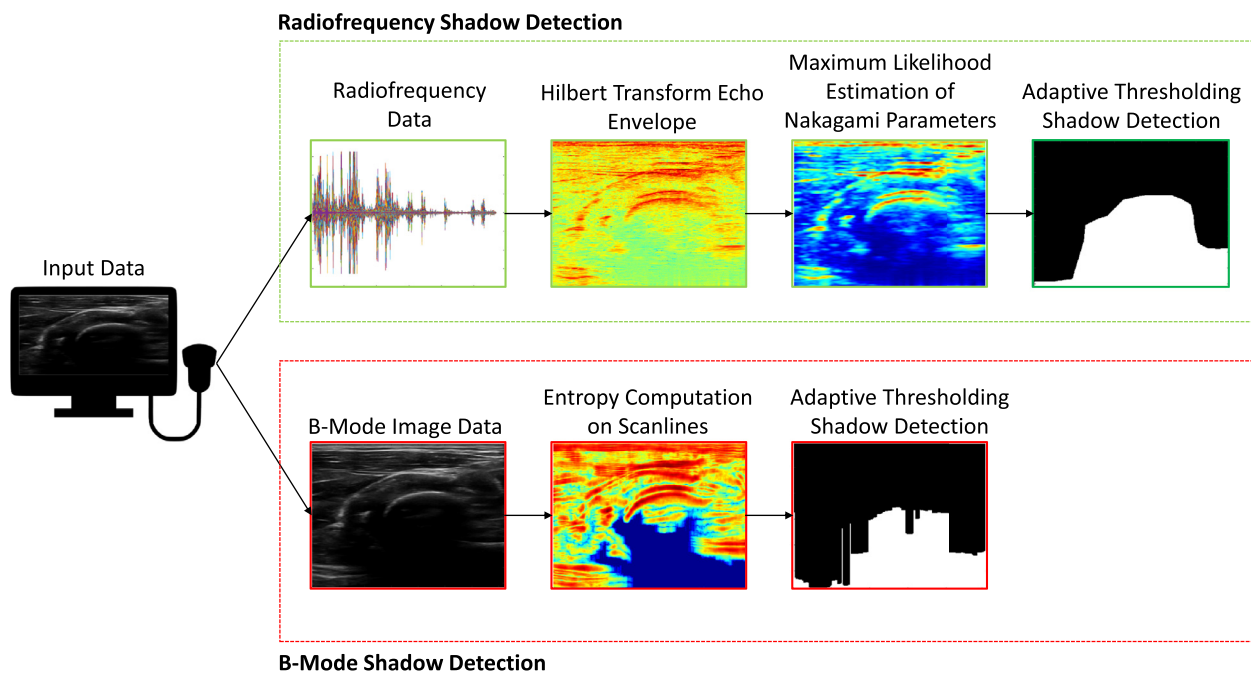
Fig. 1. Processing steps for radiofrequency (RF) and B-mode shadow detection. RF processing is used if RF data are available and involves fitting the Nakagami distribution onto the echo envelope of each RF scanline before adaptive thresholding using the Otsus method. In many cases, there may only be access to B-mode image data, for which an entropy map is computed and similar adaptive thresholding is used to detect shadows.

Table 1. Transducer properties for different imaging scenarios

Transducer	Anatomy	Frequency (MHz)	Depth (cm)	Gain	Pulse length (mm)
Linear (L14-5/38)	Forearm	11.0	5.0	50%	0.6
	Elbow	11.0	5.0	40%	0.6
	Rib cage	5.0	10.0	30%	1.7
Curvilinear (C5-2/60)	Forearm	4.0	5.0	50%	2.6
	Elbow	4.0	5.0	40%	2.6
	Rib cage	3.3	10.0	30%	5.5

12. Each scan was taken with both a curvilinear (Model C5-2/60, Ultrasonix Medical Corp., Richmond, BC, Canada) and linear (Model L14-5/38, Ultrasonix Medical Corp.) transducer. Different transducer settings were used for each anatomical region and transducer, summarized in Table 1. Shadows were expected to occur because of superficial and deep bones and from an air gap created by the lateral edges of the transducer not being in flush contact with the skin. The experiment was designed to generate a data set from various imaging scenarios to explore general shadow characteristics and to validate the versatility of the two simple shadow detection methods. The pulse lengths measured for the different transducers are reported in Table 1.

Radiofrequency speckle analysis

To analyze shadows, windows of speckle were analyzed on the RF signal. Speckle occurs from interference of randomly distributed microscopic scatterers, resulting in a granular appearance on the image. To produce B-mode images, manufacturers often employ image enhancement algorithms, such as logarithmic compression, to non-linearly alter speckle patterns. B-Mode image formation can also be manipulated by an operator by visually enhancing an image, for example, by adjusting time-gain compensation or dynamic range. Thus, the underlying speckle analysis in RF signals can provide shadow detection usable across different machines and operators. However, the original speckle pattern contains information related to the acoustic interactions in tissue (Burckhardt 1978). By analyzing the RF signal distribution, we can statistically characterize the distributions in tissue compared with shadow regions. We expect tissue to resemble speckle modeled by known distributions and expect shadow to resemble different distributions, which may be a mixture of lessened speckle resulting from the signal loss and background electronic noise. Previous studies have attempted to use despeckling methods on images containing shadows (Aysal and Barner 2007) by using filters based on a Rayleigh-like distribution. As such, even if shadow regions do not exactly resemble known speckle distributions, they may still be characterized to a sufficient extent with known distributions for a maximum likelihood fit. The fitted parameters can then be used to differentiate between shadow and non-shadow regions.

One of the first models for speckle is the one-parameter Rayleigh distribution to model the probability density of a random walk (Burckhardt 1978). The Rayleigh distribution is capable of modeling fully developed speckle, which does not occur in limited scattering (Tuthill et al. 1988). More generalized models have been applied to characterize speckle, such as the Rician, homodyned-*K* and Nakagami distributions (Destrempes and Cloutier 2010) The utility of speckle to classify tumorigenicity of breast lesions (Byra et al. 2016) or levels of liver fibrosis (Ho et al. 2012) by categorizing image regions based on the speckle pattern has been described. Shadow characterization poses a simpler problem as shadow and non-shadow regions contain significantly different speckle patterns. Thus, the Nakagami distribution expressed as

$$\Phi(x, m, \omega) = 2 \left(\frac{m}{\omega}\right)^m \frac{1}{\Gamma(m)} x^{(2m-1)} e^{\frac{-m}{\omega}x^2} \qquad (1)$$

was chosen to model speckle, where x is RF intensity, m is the shape parameter or Nakagami m parameter, ω is a scale parameter and $\Gamma(m)$ is the gamma distribution. The Nakagami distribution provides greater generality than the Rayleigh distribution while being more computationally efficient than the Rician or homodyned-*K* distribution (Destrempes and Cloutier 2010).

To characterize shadows, the raw RF data were first processed by computing the echo envelope of each scanline with a Hilbert transform. This was performed on an averaged RF signal from three image frames. This creates a pre-scan converted image, visually similar to B-mode but without filtering to alter speckle. Next, the RF image was divided into overlapped windows with a width of a single RF scanline and a length of three times the pulse length. We expect the width of a single RF scanline to be on the order of magnitude of a resolution cell, which is on the same order of magnitude as the correlation length (Wagner and Insana 1988). The window length was described in the literature to be sufficiently large to capture multiple wavelengths and scattering events while being small enough to be useful in differentiating different regions on the millimeter scale (Byra et al. 2016). Next, each window was fit to a Nakagami distribution using a maximum likelihood estimate to compute a map of Nakagami parameters m and ω, as illustrated in Figure 2.
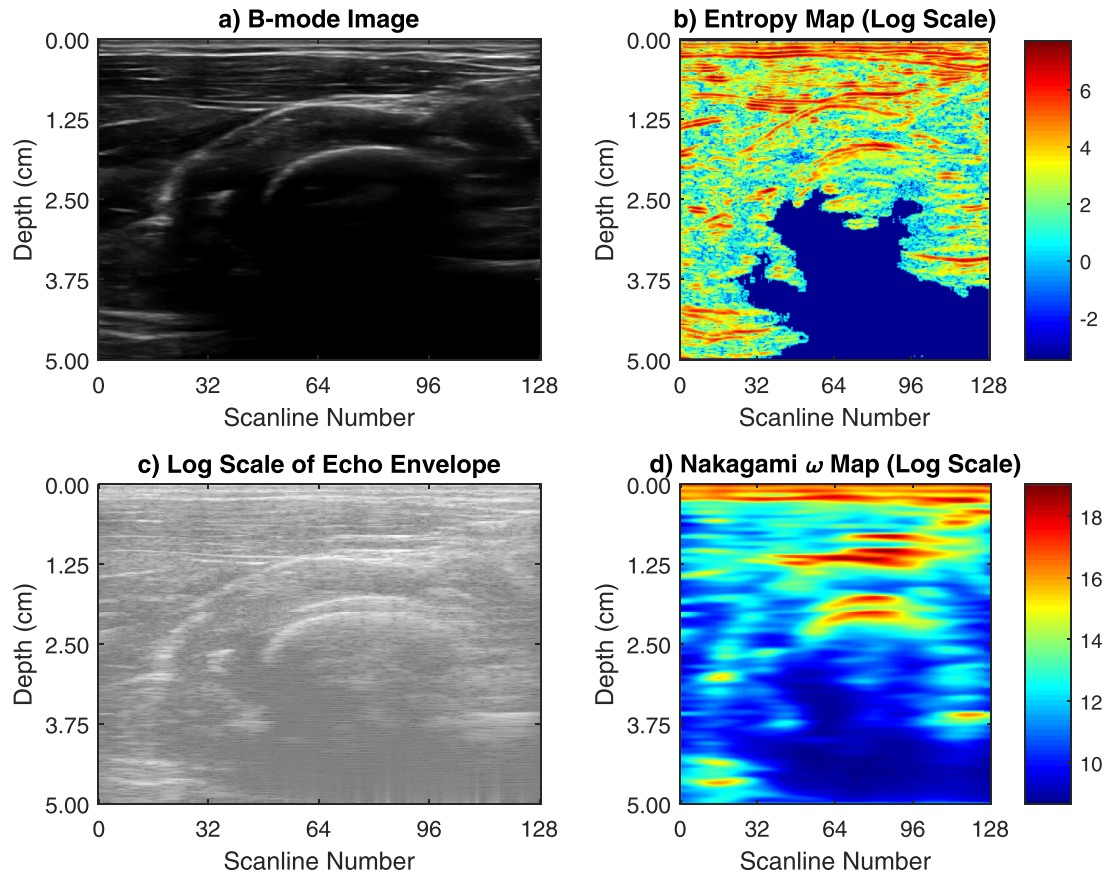
Fig. 2. Visualization of the B-mode and radiofrequency (RF) parameter maps. The (b) entropy map was computed from processing of the (a) original B-mode image and the (d) Nakagami ω map was computed from the (c) echo envelope. Note that the echo envelope contains noticeable speckle, which has been used to fit a Nakagami distribution to characterize shadow. The region at depth 2.50 cm and scanlines 32−40 is attenuation and not a shadow. This is an important distinction in shadow detection, and both maps depict the region as below a threshold to flag a shadow boundary.

Then, for each ultrasound image, the Otsu's method was applied to its Nakagami ω map to automatically compute a ω threshold for each individual image as we expect separate distributions for shadow and non-shadow regions. This was sufficient as the ω parameter is significantly different for shadow regions with abundant speckle and non-shadow regions with minimal speckle. Then, for each scanline, the axially deepest data point that is above the threshold is labeled as the shadow boundary, and all data points below are labeled as a shadow.

The Nakagami shape parameter, m, was also investigated, though there was not sufficient delineation between parameter values in shadow and non-shadow regions for this parameter to be effective in thresholding. The distributions of the two parameters are displayed for shadow and non-shadow regions in Figure 3.

B-Mode scanline analysis

Many ultrasound machines do not provide access to RF data for speckle analysis. Thus, a previous pixel gray level shadow detection method on B-mode images was modified and extended. Scanline entropy was investigated on B-mode images to characterize different types of shadows, but with the addition of adaptive thresholding of entropy to address the need for usability with minimum configuration. B-Mode analysis was performed on an averaged image from three image frames, similar to RF analysis. First, the cumulative scanline entropy is computed for each pixel, similar to the "Rupture Criterion" (Hellier et al. 2010), with approximate window size fixed as three times the pulse length, η, as defined by

$$S_{i,j} = \int_{k=1}^{3\eta} I(i-k,j) log_2 \frac{I(i-k,j)}{I(i+k,j)}$$
$$+ I(i+k,j) log_2 \frac{I(i+k,j)}{I(i-k,j)} \qquad (2)$$

where $S_{i,j}$ is the cumulative entropy at pixel i on scanline j, η is the pulse length and $I(i)$ is the gray level (0−255)
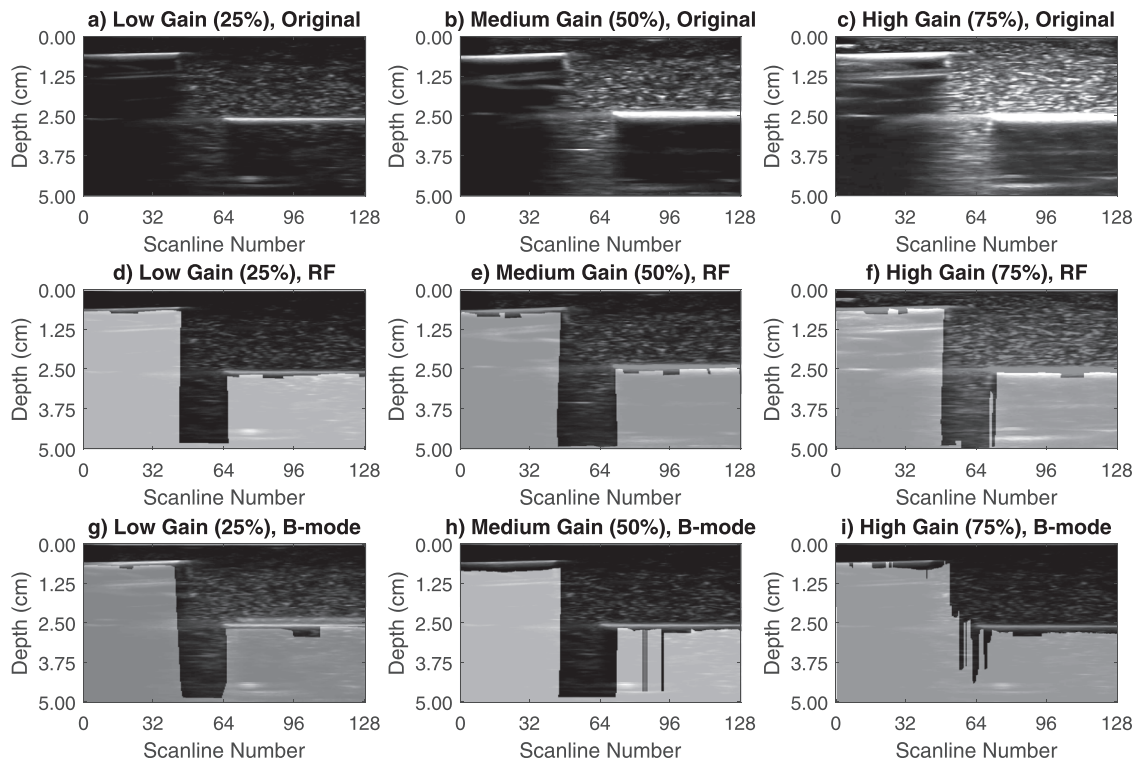
Fig. 3. Histograms of Nakagami parameters and entropy values in shadow and non-shadowing regions. The Nakagami ω and entropy distributions have a more noticeable delineation between shadowing and non-shadowing distributions compared with the Nakagami m parameter, which was not used to threshold shadow boundaries. Entropy is very minimal is continuous dark shadow regions, which is expected because of the minimal variations in pixel gray level.

of pixel (*i, j*). This is the same window size as in the RF analysis. For the case of curvilinear images, radial scanlines were linearly interpolated between the two symmetric lateral edges of the image.

Next, Otsu's method was applied onto the entropy map of each image to automatically compute a threshold entropy value, similar to RF analysis. The intuition of the threshold is different than in RF analysis. In RF analysis, the threshold separates patches of intense and minimal speckle. In B-mode analysis, the threshold separates pixels of a shadow boundary, which has high entropy, and pixels away from shadow boundary, which include shadow and non-shadow regions. Thus, shadows can be identified by finding the last pixel on a scanline with an entropy higher than the threshold, representing a bright shadow boundary.

Validation

A trained annotator (R.H.) manually outlined the boundary of the shadow regions on B-mode images. The manual regions were used as a gold standard, as manual identification is common in clinical practice and has been used in previous literature for comparison (Hellier et al. 2010). A Dice coefficient was computed to compare similarity of manual and automated shadow detection. The

manual outline was used to define four regions for classification of statistical parameters: a non-shadow region above the boundary, a shadow region below the boundary, a "transition region," which is a window defined as three pulse lengths long axially below the boundary, and a "deep shadow region," which is the data below the transition region. The validation was repeated with the RF and entropy window increased and decreased by 50%. The Ljung−Box Q-test was used to measure residual autocorrelation of the Dice coefficients. A Wilcoxon rank sum test has been performed between Nakagami parameter values in shadow and non-shadow regions and between entropy values in shadow and non-shadow regions.

As an initial experiment, a gelatin phantom was created with slits of wood embedded at 0.75 and 2.50 cm to create a region of shallow and deeper shadows on both edges of the phantom. The gain was varied, and both RF and B-mode methods were employed to test the feasibility of the methods on a clearly visible shadow, illustrated in Figure 4. When compared with manual segmentation, all detected shadows resulted in a Dice coefficient >0.95, with the lowest score being the entropy method applied on a high-gain image. This provides support that extreme operator adjustments on the B-mode image may affect pixel gray level detection methods more than RF methods.
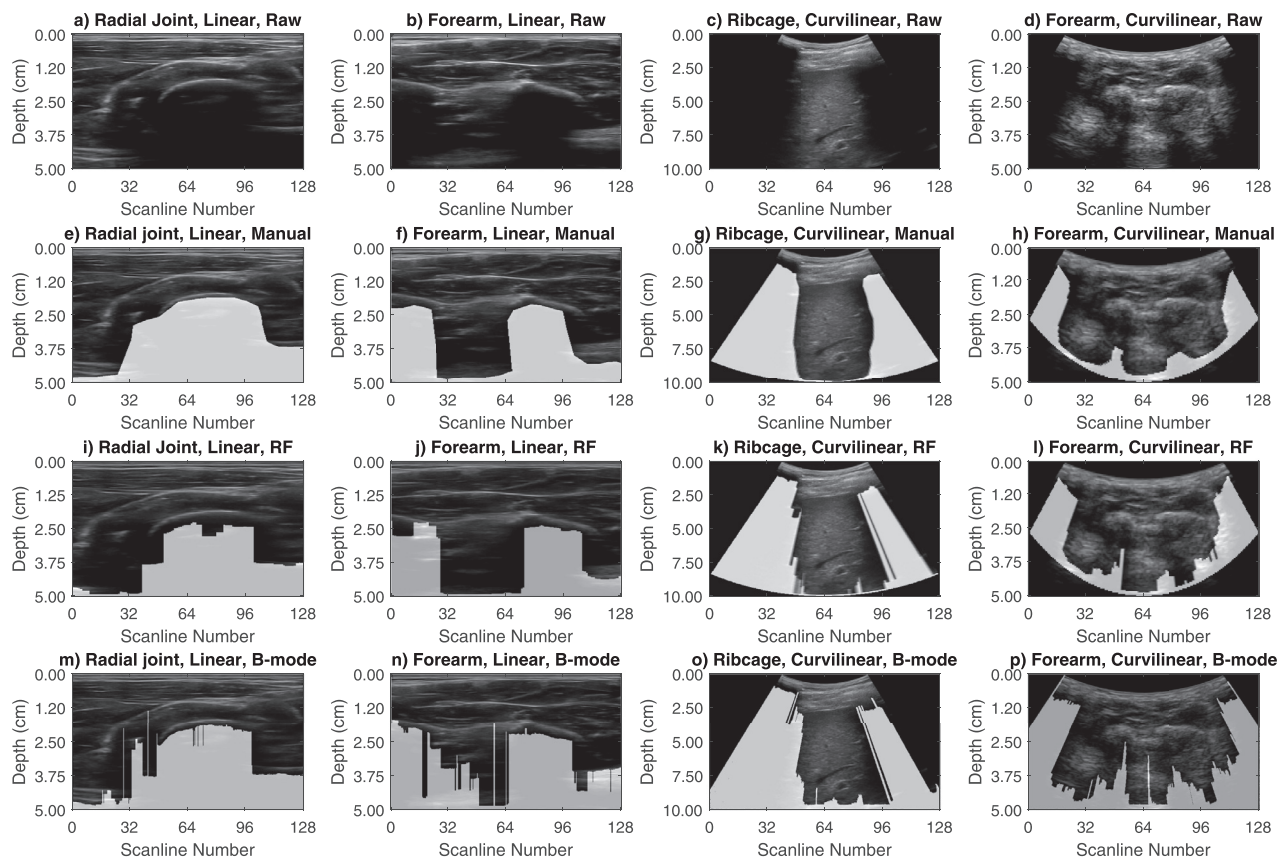
Fig. 4. Images of both radiofrequency (RF) and B-mode shadow detection performed on a gelatin phantom with two wooden slits embedded at depths of 0.75 and 2.50 cm. The phantom was made to simulate shallow, deep and non-shadow regions. The methods were capable of shadow detection with a high accuracy (Dice coefficient >0.95), though noticeable errors were present at high-gain images for the B-mode method. This is expected as B-mode methods rely on pixel gray level, which may vary with operator settings.

RESULTS

Examples of shadows detected by both methods are highlighted in gray in Figure 5 in different shadow detection scenarios. The Dice coefficients for both methods for different anatomy and transducers are listed in Table 2. The Dice coefficients (mean ± standard deviation) were 0.90 ± 0.07 and 0.87 ± 0.08 for RF and B-mode methods. Manual annotation was repeated five times with a mean Dice coefficient of 0.92 ± 0.02 for all images and transducers. The Dice coefficient did not change by more than 0.03 when the window size was varied by 50%.

With the benefit of a varied data set, general statistics of shadows can be analyzed, as summarized in Tables 3 and 4. The distributions of Nakagami parameters and entropy for the different regions are illustrated in Figure 3. For shadow detection, the parameters differentiating a shadow and non-shadow are of particular interest. Shadows were observed to have a mean Nakagami ω parameter of 4.14 ± 0.40 and a mean entropy of

1.03 ± 0.29, whereas non-shadows were observed to have a mean ω of 6.24 ± 0.92 and mean entropy of 2.20 ± 0.81. Wilcoxon rank sum p values were <0.002 between Nakagami ω parameter distributions in shadow and non-shadow regions and <0.001 between entropy distributions in shadow and non-shadow regions, indicating that shadow and non-shadow regions have statistically different distributions for Nakagami ω parameters and entropy. The values of entropy and Nakagami ω are consistent across different transducers and anatomical regions. The variance of entropy and Nakagami ω in one imaging region and transducer setting is less than the variance across different regions and transducers for shadows and non-shadows.

DISCUSSION

The RF and B-mode shadow detection methods developed achieved a Dice similarity coefficient comparable to that of manual detection for all anatomy and transducer types ($p < 0.025$). The previous studies using
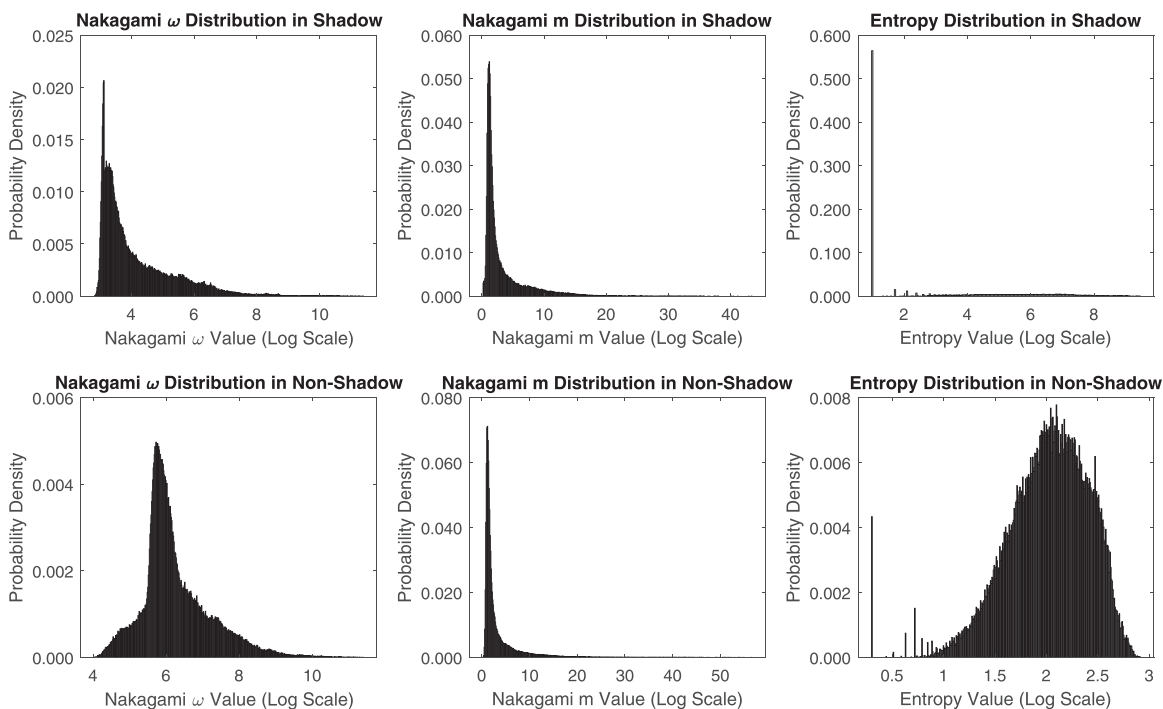
Fig. 5. Comparison of the original B-mode images, the detected shadows manual detection, radiofrequency (RF) detection and B-mode detection. Both detection methods perform similarly to manual detection. Both methods perform slightly less accurately on curvilinear images, likely because of the reduced resolution from interpolation of the scanlines. Most errors in RF detection occur near the shadow boundary, likely because of the transitioning speckle from non-shadow to shadow.

Table 2. Mean Dice coefficients for different imaging scenarios

		Radiofrequency	B-Mode
Linear (L14-5/38)	Forearm	0.91 ± 0.05*	0.89 ± 0.06
	Elbow	0.94 ± 0.06	0.90 ± 0.07
	Rib cage	0.87 ± 0.09	0.84 ± 0.06
Curvilinear (C5-2/60)	Forearm	0.89 ± 0.05	0.86 ± 0.08
	Elbow	0.93 ± 0.04	0.90 ± 0.09
	Rib cage	0.83 ± 0.08	0.83 ± 0.10
Mean	All anatomy	0.90 ± 0.07	0.87 ± 0.08

* Mean ± standard deviation.

B-mode entropy reported a mean Dice coefficient of 0.91 ± 0.07 between manual annotators (Hellier et al. 2010). An important feature of shadow detection is its ability to differentiate between a shadow and simply high attenuation of the signal. Both scenarios result in an eventual loss of signal. Shadow detection, however, has a characteristic high gray level shadow boundary before a significant loss in signal, compared with gradual signal losses in attenuation. The high Dice similarity coefficient indicates that both methods were capable of this distinction. This is also illustrated in Figure 5, where regions of low gray level without a bright shadow boundary were correctly labeled as a non-shadow. The high accuracy supports the versatility of the detection method as both

methods are able to identify shadows across different anatomy and transducers with a minimum configuration.

For a general observation for shadows, the computed Nakagami ω parameters of all manually outlined shadows indicate that there is a statistically significant difference between shadow and non-shadow regions, regardless of anatomy and transducer and even with the error in the transition regions considered. The speckle and its statistics from shadows are thus distinct from the speckle created by tissue, muscle or fat. This observation can be utilized in the future for further analysis of shadows.

In RF detection, both false positive and false negative errors most frequently occurred immediately below a shadow boundary as opposed to B-mode detection, where errors were in various regions. To study the frequent areas of error further, the "transition region" immediately below a manually annotated shadow boundary and a "deep shadow region" below the transition region was investigated. The Nakagami ω parameters of transition regions of all anatomy and transducers were within a standard deviation of those of both shadow and non-shadow regions. The deeper shadow regions were observed to have a lower Nakagami ω parameter than shadow regions and with a lower standard deviation, as summarized in Table 3. The spread of the speckle also significantly decreases after the transition region. This indicates that

Table 3. Mean Nakagami ω and entropy values of different anatomy, transducer and shadowing region*

	Linear (L14-5/38)			Curvilinear (C5-2/60)		
	Forearm	Elbow	Rib cage	Forearm	Elbow	Rib cage
Nakagami ω (log scale)						
Shadow	$4.15 \pm 0.45^{\dagger}$	4.18 ± 0.45	4.04 ± 0.42	4.22 ± 0.32	4.19 ± 0.40	4.08 ± 0.37
Non-shadow	6.19 ± 0.96	6.49 ± 0.97	6.29 ± 0.95	6.54 ± 0.88	6.29 ± 1.04	5.64 ± 0.71
Transition	4.94 ± 0.62	5.36 ± 0.62	4.96 ± 0.38	5.26 ± 1.02	5.37 ± 0.99	4.59 ± 0.92
Deep shadow	4.13 ± 0.43	4.16 ± 0.43	4.03 ± 0.41	3.93 ± 0.20	4.09 ± 0.30	4.03 ± 0.26
Entropy (log scale)						
Shadow	0.92 ± 0.22	1.10 ± 0.36	1.04 ± 0.27	1.06 ± 0.28	0.96 ± 0.21	1.10 ± 0.37
Non-Shadow	2.34 ± 0.96	2.34 ± 0.80	2.14 ± 0.82	1.67 ± 0.82	1.75 ± 1.14	1.88 ± 0.42
Transition	2.45 ± 0.62	2.56 ± 0.53	2.15 ± 0.51	2.18 ± 1.21	1.93 ± 1.10	1.99 ± 1.10
Deep shadow	0.71 ± 0.43	0.89 ± 0.26	0.92 ± 0.40	0.98 ± 0.21	0.82 ± 0.19	1.04 ± 0.26

* Values are consistent among different transducers and anatomical regions. The variance of entropy and Nakagami ω in one imaging region and transducer setting is less than the variance across different regions and transducers for shadows and non-shadows.
† Mean $\pm$ standard deviation.

Table 4. Mean Nakagami ω and entropy values of all anatomy and transducers for different shadowing regions

	Mean Nakagami ω (log scale)	Mean entropy (log scale)
Shadow	4.14 ± 0.40*	1.03 ± 0.29
Non-shadow	6.24 ± 0.92	2.02 ± 0.81
Transition	5.08 ± 0.77	2.21 ± 0.84
Deep shadow	4.06 ± 0.34	0.89 ± 0.27

* Mean $\pm$ standard deviation.

the transition region cannot be fully distinguished from either a shadow or non-shadow and presents as if it is statistically similar to the two. This is likely the cause of the errors, as the speckle distribution is much more consistent in the deep shadow regions than in any other region. Physically, speckle interactions appear to gradually lessen after the brightest point on a scanline, possibly because of incomplete total reflection at a boundary. The boundary is thus is not an instantaneous division between non-shadow and shadow; rather, there is a transition region with statistics between a shadow and non-shadow before the speckle fully resembles a shadow.

In the transition region of B-mode images, the entropy values were similar but consistently higher than the non-shadow values. This is expected as entropy is highest when there is the greatest change in pixel gray level, which occurs at a shadow boundary, even with a non-instantaneous non-shadow to shadow transition. However, the averaged entropy of all non-shadow regions has a greater spread than the Nakagami parameters, likely because of the differing operator settings used. Thus, B-mode detection may not be as consistent as RF detection.

Limitations

In our study, although a range of frequencies and equipment were used, the parameters were still limited, and not all combinations were explored. To further

validate the detection method, future work should include a more extensive investigation of these parameters, such as with a random parameter grid search, to provide more support for widespread clinical use.

As both RF and B-mode images search for a threshold for the shadow boundary, it is possible to misinterpret a reverberation artifact as the beginning of a shadow. Reverberation at a shadow boundary would cause a similar bright region followed by a dark region, which visually appears like a shadow boundary despite being an artifact in a shadow region. This is a limitation of our method, and future work, including integration of reverberation identification, such as identifying echo time duration to determine what pulses correspond to anatomical interaction (Win et al. 2010), would be required to reduce reverberation errors.

There is a limitation with analysis using the Nakagami distribution in that the fitted Nakagami distribution to model scatterers changes with transducer frequency. It has been observed that in the frequency range $36-58$ MHz, the Nakagami m parameter decreased near the theoretical lower limit compared with a higher Nakagami m parameter value at a 10-MHz signal (Cloutier et al. 2004). This was reported to be caused by the spatial organization of the cells being "on the order of a fraction of the wavelength," and a Nakagami distribution cannot model the scatterers of red blood cells at this frequency. Because of this and the limitations of the equipment used in our study, we cannot conclude that shadow detection with Nakagami analysis will be accurate at higher frequencies beyond the values tested. Future studies are required to analyze the performance of shadow detection at higher frequencies. Diagnostic ultrasound commonly uses a frequency range of $2-15$ MHz (Jensen 2007), and higher frequencies are limited to sub-specialty cases such as optical ultrasound (Pavlin et al. 1992). Shadow detection is expected be applicable in most use cases without issues arising from the high-frequency behavior of the Nakagami distribution.

There is a limitation to diagnostic use of the proposed shadow method in cases where acoustic shadowing does not exhibit the characteristic bright boundary followed by a dark region. In cases where there is partial or incomplete shadowing, such as small calcifications in the placenta (Abramowicz and Sheiner 2008), there is a resemblance to a shadow, where the calcification is brighter and the region below is noticeably darker, but not with a brightness difference as extreme as the shadowing from the ulna, and the regions below retain speckle similar to tissue. Although calcifications are pathologically important to recognize, the proposed shadow detection method would likely be unable to detect the partial shadowing from these calcifications. The proposed method would be applicable only in cases of more complete shadowing, which would still be practical for significant gall and kidney stones, for example.

Shadows have been defined qualitatively (Kremkau and Taylor 1986) as a sudden loss of signal and brightness. The observed transition region in this study suggests that the qualitative definition of a shadow may be insufficient for accurate detection. One algorithm may detect the shadow starting immediately after the brightest location, or another may use a convention such as a full width at half-maximum to define where the signal has sufficiently low gray level to resemble the start of a shadow. A decision point is required for a clear definition of where a shadow begins to improve shadow detection accuracy, both from a signaling perspective for image processing and from a visual perspective for manual inspection.

The findings in this study have several implications. First, the statistics of acoustic shadows have been investigated on a data set with shadows occurring from multiple scenarios as opposed to specific cases where shadows are observed. This provided a more generalizable observation that shadows can be characterized by distinctive speckle distributions in different types of anatomy and equipment and that there exists a transition region before the loss of speckle in a shadow. Second, the shadow detection methods had high accuracy, indicating that the same shadow detection method can be used with different transducers or imaging locations. In future studies, the speckle statistics obtained can be used to develop additional models for anatomical features containing shadows. In machine learning algorithms, an initial network could be used with the shadow detection methods presented. Future studies would also have to take into consideration the most frequent source of error of shadow detection, the shadow boundary.

CONCLUSIONS

Acoustic shadows from different imaging scenarios were investigated. RF and B-mode methods requiring only the transducer pulse length as the input parameter were developed for acoustic shadow detection. Compared with manual detection, the methods achieved a Dice similarity coefficient within the range obtained by manual observers. The work focused on applying shadow detection and statistical analysis to a varied data set of three different anatomical locations and two different transducers to provide a representative understanding of general acoustic shadows. The statistics of acoustic shadows indicate that shadows contain a distinct speckle distribution compared with non-shadows and that speckle characteristics transition at the shadow boundary. The statistical findings on shadows can aid interpretation of ultrasound images in the future using speckle analysis. The versatility of the shadow detection method gives it the potential to improve the interpretation of ultrasound images with shadow artifacts or to serve as a pre-processing step for machine learning methods.

REFERENCES

Abramowicz JS, Sheiner E. Ultrasound of the placenta: A systematic approach. Part I. Imaging. Placenta 2008;29:225–240.

Aysal TC, Barner KE. Rayleigh-maximum-likelihood filtering for speckle reduction of ultrasound images. IEEE Trans Med. Imaging 2007;26:712–727.

Bouhemad B, Brisson H, Le-Guen M, Arbelot C, Lu Q, Rouby JJ. Bedside ultrasound assessment of positive end-expiratory pressure-induced lung recruitment. Am J Resp Crit Care Med 2011; 183:341–347.

Burckhardt CB. Speckle in ultrasound B-mode scans. IEEE Trans Sonics Ultrason 1978;25:1–6.

Byra M, Nowicki A, Wróblewska-Piotrzkowska H, Dobruch-Sobczak K. Classification of breast lesions using segmented quantitative ultrasound maps of homodyned K distribution parameters. Med Phys 2016;43:5561–5569.

Cloutier G, Savery MDD, Garcia D, Durand LG, Foster SF. Non-Gaussian statistics and temporal variations of the ultrasound signal backscattered by blood at frequencies between 10 and 58 MHz. Acoust Soc Am 2004;116:566–577.

Destrempes F, Cloutier G. A critical review and uniformized representation of statistical distributions modeling the ultrasound echo envelope. Ultrasound Med Biol 2010;36:1037–1051.

Galiano K, Obwegeser AA, Bodner G, Freund M, Maurer H, Kamelger FS, Schatzer R, Ploner F. Ultrasound guidance for facet joint injections in the lumbar spine: A computed tomography-controlled feasibility study. Anesth Analg 2005;101:579–583.

Ghose S, Oliver A, Mitra J, Martí R, Lladó X, Freixenet J, Sidibé D, Vilanova JC, Comet J, Meriaudeau F. A supervised learning framework of statistical shape and probability priors for automatic prostate segmentation in ultrasound images. Med Image Anal 2013; 17:587–600.

Good LI, Edell SL, Soloway RD, Trotman BW, Mulhern C, Arger PA. Ultrasonic properties of gallstones: Effect of stone size and composition. Gastroenterology 1979;77:258–263.

Hellier P, Coupé P, Morandi X, Collins DL. An automatic geometrical and statistical method to detect acoustic shadows in intraoperative ultrasound brain images. Med Image Anal 2010;14:195–204.

Hetherington J, Lessoway V, Gunka V, Abolmaesumi P, Rohling R. SLIDE: Automatic spine level identification system using a deep convolutional neural network. Int J Computer Assist Radiol Surg 2017;12:1189–1198.

Ho MC, Lin JJ, Shu YC, Chen CN, Chang KJ, Chang CC, Tsui PH. Using ultrasound Nakagami imaging to assess liver fibrosis in rats. Ultrasonics 2012;52:215–222.

Jensen JA. Medical ultrasound imaging. Prog Biophys Mol Biol 2007;93:153–165.

Karamalis A, Wein W, Klein T, Navab N. Ultrasound confidence maps using random walks. Med Image Anal 2012;16:1101–1112.

Kremkau FW, Taylor KJ. Artifacts in ultrasound imaging. J Ultrasound Med 1986;5:227–237.

Milletari F, Ahmadi SA, Kroll C, Plate A, Rozanski V, Maiostre J, Levin J, Dietrich O, Ertl-Wagner B, Bötzel K, Navab N. Hough-CNN: Deep learning for segmentation of deep brain regions in MRI and ultrasound. Comput Vis Image Understand 2017;164:92–102.

Pavlin CJ, Ritch R, Foster FS. Ultrasound biomicroscopy in plateau iris syndrome. Am J Ophthalmol 1992;113:390–395.

Sippel S, Muruganandan K, Levine A, Shah S. Review article: Use of ultrasound in the developing world. Int J Emerg Med 2011;4:72.

Tuthill TA, Sperry RH, Parker KJ. Deviations from Rayleigh statistics in ultrasonic speckle. Ultrason Imaging 1988;10:81–89.

Wagner RF, Insana MF. Fundamental correlation lengths of coherent speckle in medical ultrasonic images. IEEE Trans Ultrason Ferroelectr Freq Control 1988;35:34–44.

Win KK, Wang J, Zhang C, Yang R. Identification and removal of reverberation in ultrasound imaging. In: Proceedings of the 2010 5th IEEE Conference on Industrial Electronics and Applications: ICIEA 2010. Piscataway, NJ. IEEE; 2010.